JOURNAL OF GEOPHYSICAL RESEARCH, VOL. 115, A05206, doi:10.1029/2009JA015006, 2010

Click Here for Full Article

Thermal ion upflow in the cusp ionosphere and its dependence on soft electron energy flux

J. K. Burchill,[1] D. J. Knudsen,[1] J. H. Clemmons,[2] K. Oksavik,[3] R. F. Pfaff,[4] C. T. Steigies,[5] A. W. Yau,[1] and T. K. Yeoman[6]

Received 19 October 2009; revised 25 November 2009; accepted 29 December 2009; published 14 May 2010.

[1] We investigate the origin of low-energy (E_k < 10 eV) ion upflows in Earth's low-altitude dayside cusp region. The Cusp-2002 sounding rocket flew from Ny Ålesund, Svalbard, on 14 December 2002, carrying plasma and field instrumentation to an altitude of 768 km. The Suprathermal Ion Imager, a two-dimensional energy/arrival angle spectrograph, observed large (>500 m s^{-1}) ion upflows within the cusp at altitudes between 640 km and 768 km. We report a significant correlation between ion upflow and precipitating magnetosheath electron energy flux in this altitude range. There is only very weak correlation between upflow and wave power in the VLF band. We find a small negative correlation between upflow and the magnitude of the DC electric field for fields less than about 70 mV m^{-1}. The apparent relation between upflow and electron energy flux suggests a mechanism whereby ions are accelerated by parallel electric fields that are established by the soft electrons. Significant ion upflows are not observed for electron energy fluxes less than about 10^{10} eV cm^{-2} s^{-1}. The lack of correspondence between $|\vec{E}|$ and upflow on the one hand, and wave power and upflow on the other, does not rule out these processes but implies that, if operating, they are not local to the measurement region. We also observe narrow regions of large ion downflow that imply either a rebalancing of the ionosphere toward a low-T_e equilibrium during which gravity dominates over the pressure gradients or a convection of the upflowing ions away from the precipitation region, outside of which the ions must fall back into equilibrium at lower altitudes.

Citation: Burchill, J. K., D. J. Knudsen, J. H. Clemmons, K. Oksavik, R. F. Pfaff, C. T. Steigies, A. W. Yau, and T. K. Yeoman (2010), Thermal ion upflow in the cusp ionosphere and its dependence on soft electron energy flux, *J. Geophys. Res.*, *115*, A05206, doi:10.1029/2009JA015006.

1. Introduction

[2] In this paper we investigate the bulk upflow of low-energy (E_k < 10 eV) thermal ions in the low-altitude northern cusp. Observational and theoretical research from the 1960s to present-day have established that the ionosphere is a significant source of ions for the magnetosphere [*Nishida*, 1966; *Banks and Holzer*, 1969; *Shelley et al.*, 1972; *Hoffman and Dodson*, 1980; *Shelley et al.*, 1982; *Horwitz*, 1982; *Waite et al.*, 1985; *Lockwood et al.*, 1985; *Cladis*, 1986; *Chappell*, 1988; *Abe et al.*, 1993] (see, for example, the review by *Horwitz and Moore* [1997]). At high altitudes (>2000 km), the classical polar wind (the high-latitude flow of ionospheric thermal plasma into the magnetosphere on open geomagnetic field lines) supplies the magnetosphere with primarily H^+, He^+ and O^+ ions, with bulk speeds reaching gravitational escape speed [*Abe et al.*, 1993] (see also the reviews by *Yau and Andre* [1997] and *Yau et al.* [2007]). Moreover, ion acceleration by plasma waves and parallel electric fields directly gives rise to suprathermal outflowing ions in the form of conics and field-aligned beams, respectively [*Sharp et al.*, 1977; *Ghielmetti et al.*, 1978; *Gorney et al.*, 1981; *Carlson et al.*, 1998; *André et al.*, 1998; *Bouhram et al.*, 2002]. *Lockwood et al.* [1985], *Tsunoda et al.* [1989] and others have established what has become known as the "Cleft Ion Fountain," a narrow-latitude source of heavy ion outflow in the cusp/cleft.

[3] The high-altitude outflows are regulated in part by the supply of thermal plasma from below, via the magnetic field-aligned motion of the cold, dense *F* region and topside ionospheric plasma at midlatitudes and high latitudes (see the review by *Moore et al.* [1999, and references therein]).

[1]Department of Physics and Astronomy, University of Calgary, Calgary, Alberta, Canada.
[2]Space Science Applications Laboratory, Aerospace Corporation, El Segundo, California, USA.
[3]Department of Arctic Geophysics, University Centre in Svalbard, Longyearbyen, Norway.
[4]Space Weather Laboratory, NASA Goddard Space Flight Center, Greenbelt, Maryland, USA.
[5]Institut für Experimentelle und Angewandte Physik, Christian-Albrechts-Universität zu Kiel, Kiel, Germany.
[6]Department of Physics and Astronomy, University of Leicester, Leicester, UK.

Copyright 2010 by the American Geophysical Union.
0148-0227/10/2009JA015006

Ground-based radars and orbiting spacecraft have routinely observed low-altitude (<2000 km) thermal ion upflows at midlatitudes and high latitudes reaching speeds of up to 1 km s^{-1}, and occasionally greater [e.g., *Tsunoda et al.*, 1989; *Wahlund and Opgenoorth*, 1989; *Yeh and Foster*, 1990; *Loranc et al.*, 1991; *Wahlund et al.*, 1992; *Semeter et al.*, 2003; *Ogawa et al.*, 2009]. A number of rocket experiments have reported large upflows at altitudes below 1000 km [*Bering et al.*, 1975; *Lynch et al.*, 2007]. Following convention we use the term upflow to refer to upward bulk motion of ions with speeds less than the escape speed, whereas outflow signifies speeds greater than escape speed. In the literature, upflowing ions are often classified into thermal and suprathermal components, and within the thermal component the polar wind and auroral bulk upflow are the dominant types.

[4] A number of mechanisms are known to be capable of causing ion upflow. (1) Collisional $\vec{E} \times \vec{B}$ convection flow energy is dissipated as heat (frictional heating) in the *E* region, causing a rise in ion temperature and consequently an expansion of the ionosphere [e.g., *Loranc and St.-Maurice*, 1994]. (2) Soft electron (<1 keV) precipitation and/or heat conduction increases the temperature of the ionospheric electrons, enhancing the ambipolar electric field which then accelerates ions upward [*Whitteker*, 1977; *Liu et al.*, 1995; *Horwitz and Moore*, 1997]. (3) Anisotropic ion heating by plasma waves (broadband extremely low frequency (BBELF) waves, for example, generated by convective velocity shear) can lead to upflow via the magnetic mirror force [*Ganguli et al.*, 1994]. (4) Precipitation of heavy ions from the ring current can drive high-speed midlatitude heavy ion upflows [*Yeh and Foster*, 1990]. (5) Other mechanisms have been proposed for generating and sustaining electric fields in the direction parallel to the geomagnetic field [e.g., *Kagan and St.-Maurice*, 2005, and references therein]. These electric fields can directly drive thermal ion upflow. The consequence of all these mechanisms is that they can supply fresh plasma to the source regions of high-altitude ion outflow [e.g., *Horwitz and Moore*, 1997].

[5] There is still some controversy on the role of electron precipitation in driving ion upflow. *Moen et al.* [2004] provided strong evidence for low-energy particle precipitation as the principal driver for ion upflow in the low-altitude cusp based on coordinated ground-based radar and optical measurements of poleward moving auroral forms and ion upflow. They emphasized the transient nature of the upflow and electron precipitation, and argued that both are signatures of reconnection. They suggested that all ion outflow events start ultimately in the *F* region ionosphere. *Ogawa et al.* [2000] presented simultaneous radar observations of ion upflow that were consistent with a combination of electron precipitation and the mirror force (via transverse ion acceleration from waves) as the causes of upflow. *Lynch et al.* [2007] presented SIERRA rocket observations of ion upflows up to 2 km s^{-1} in the cusp/cleft. Using simulations from the TRANSCAR ionospheric model, they argued that the upflow was driven by soft electron precipitation. On the other hand, *Frederick-Frost et al.* [2007] confirmed the link between BBELF and ion heating in a region of ion upflow in the cusp/cleft ionosphere from in situ observations on the SERSIO sounding rocket between 520 and 780 km. During a period of ion upflow on the nightside poleward edge of the auroral zone, *Semeter et al.* [2003] observed no enhancement in either electron or ion plasma temperatures, and speculated that neither soft electron precipitation nor magnetospheric electron heat flux could explain the upflow. Using observations from the FAST satellite at 4000 km altitude, *Strangeway et al.* [2005] found a higher correlation between upward ion flux and precipitating electron density than upward ion flux and Poynting flux in the high-latitude, high-altitude dayside cusp, although they recommended using Poynting flux as an indicator of upflow when particle measurements are not available. The investigation by *Zheng et al.* [2005], using observations from the Polar satellite at 6000 km altitude, qualitatively corroborated the findings of *Strangeway et al.* [2005], although their scaling laws have different powers. *Seo et al.* [1997] found significant correlations between ion upflow velocity and the electron and ion temperatures, and suggested that their observations were consistent with an ambipolar electric field driver, although they could not rule out contributions from ion frictional heating. *Séran et al.* [2007] presented Demeter observations of regions of O^+ upflow in the midnight auroral zone during the magnetic storm of 7–8 November 2004, from which they determined that the upflowing ions were colder than the ambient ions. *Knudsen et al.* [1998] demonstrated positive correlations between core (i.e., thermal and suprathermal) ion energization and both electron directional particle flux and BBELF wave power measurements from the Freja satellite at altitudes between 1400 and 1700 km. They reported thresholds in both electron flux and wave power for the onset of ion energization.

[6] This article focuses on low-altitude thermal ion upflow observations gathered on a sounding rocket in proximity to the dayside cusp. What distinguishes this study from those based on radars is the combined in situ measurement of ion upflow and the precipitating electrons, as well as the high temporal and spatial resolutions of the measurements. Another distinctive element of this study is that our ion measurements, in contrast to those obtained from devices such as the ion drift meter [e.g., *Heelis and Hanson*, 1998, and references therein], are derived from a recently developed technique based on an imaging charged particle analyzer that measures ion two-dimensional energy/angle distributions. These ion distributions allow us to validate an analyzer model that assists in the derivation of the ion upflow and temperature measurements, and that we use to quantify the measurement uncertainties.

[7] As will be shown, the observations provide compelling evidence for precipitating soft electron energy flux as a driver of the observed topside cusp ion upflow. In section 2 we provide an overview of the observations. Section 3 presents the results of our investigation, which are discussed and summarized in section 4. Details on the ion image analysis techniques, including error analysis, are presented in Appendix A.

2. Observations

[8] The Cusp-2002 (NASA 35.033) mission was a coordinated study of cusp and boundary layer electrodynamics and charged particle acceleration by a sounding rocket and ground-based radars [*Pfaff et al.*, 2004]. Cusp-2002 was

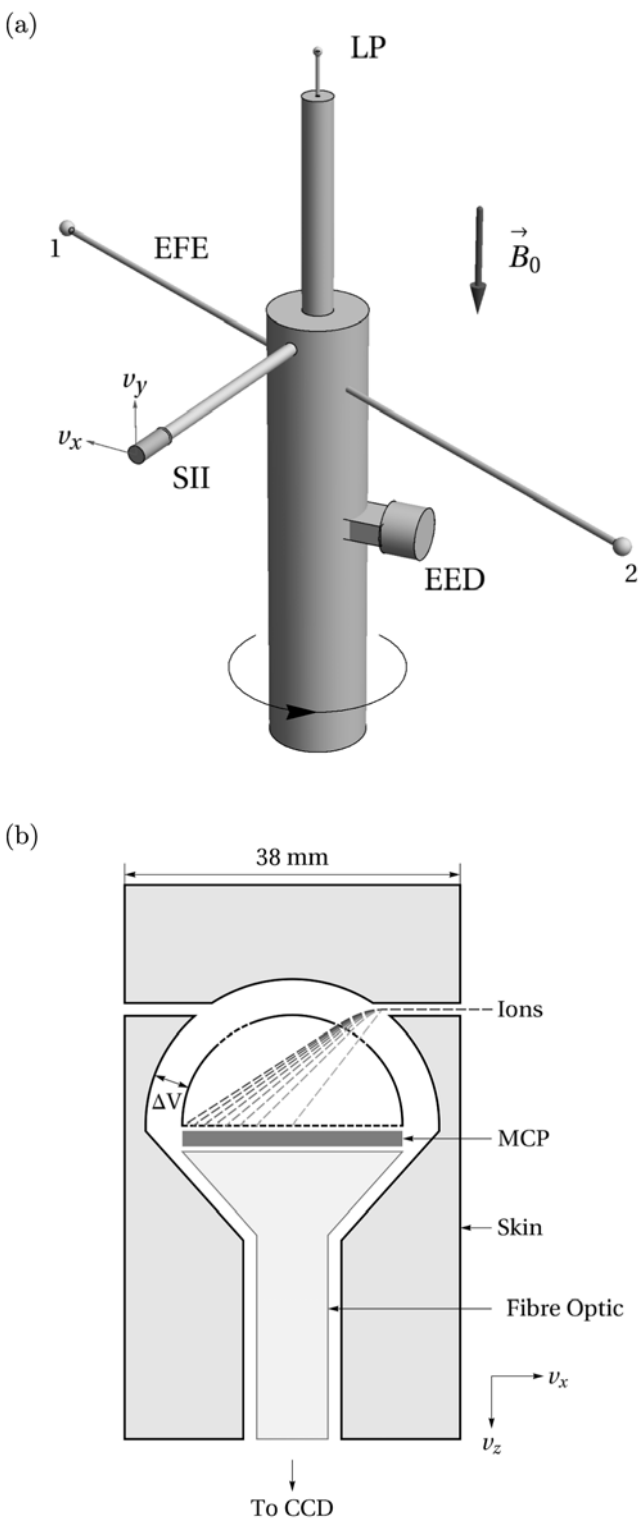

Figure 1. (a) Schematic of Cusp-2002 payload showing the locations of the SII, EED, LP, and EFE antenna spheres 1 and 2 (not to scale). An attitude control system maintains alignment of the payload rotation axis to within a few degrees of $\vec{B}_0$. (b) Cross-sectional illustration of the SII analyzer (not to scale). The analyzer is a figure of revolution about the v_z axis.

launched at 1116:48 UT (~1300–1400 MLT) on 14 December 2002 into the topside cusp ionosphere during a period of predominantly southward ($B_{z,\mathrm{GSM}}$ ~ −10 to −15 nT) and dawnward ($B_{y,\mathrm{GSM}}$ ~ −10 nT) interplanetary magnetic field (IMF). The payload achieved an apogee of approximately 768 km at the time 493 s after launch. The rocket payload traversed ~6° of magnetic latitude and ~20° of magnetic longitude in a southwesterly direction. An attitude control system (ACS) was used to orient the payload rotational axis to within a few degrees of the local geomagnetic field direction and to maintain the payload spin period at 2.2 s. The Wideband Imaging Camera on the IMAGE satellite observed steady auroral UV emissions which confirm that the payload traversed the postnoon aurora.

2.1. Instrumentation

[9] In situ measurements that are available for this study include low-energy (0–25 eV) ions from the Suprathermal Ion Imager (SII), energetic (0.01–30 keV) electron distributions from a top hat electrostatic analyzer (Energetic Electron Detector (EED)), DC- and AC-coupled electric field measurements (0–10 kHz) from the Electric Field Experiment (EFE), and electron density and temperature from a swept-bias spherical Langmuir probe (LP). The layout of the SII, the EED, the LP, and the EFE (spheres 1 and 2 only) sensors on the payload are illustrated schematically in Figure 1a (not to scale).

[10] The Cusp-2002 SII (Figure 1b) analyzed core ion energy distributions throughout the flight. In contrast to spectrometers such as the top hat [e.g., *Carlson et al.*, 1982], which scan through the range of kinetic energies, or devices based on integral measurements such as the ion drift meter [e.g., *Heelis and Hanson*, 1998], the SII is an energy/angle-of-arrival analyzer that produces images representing 2-D slices through the ion energy distribution function. These ion images are the basis for measuring ion upflows and temperatures on this flight. A full description of the SII design and operation can be found in the work by *Knudsen et al.* [2003]. In brief, ions within the sensor's field of view (~5° × 360°) enter and cross the gap between the two hemispherical electrodes (Figure 1b). A constant voltage ΔV applied across the electrodes creates a radial electric field which disperses the ions according to their kinetic energy per unit charge: ions with greater kinetic energy reach the microchannel plate (MCP) intensifier at greater radii. The intensified signal is projected onto a phosphor screen (not shown), which is connected to a charge-coupled device (CCD) by a coherent fibre optic cable. A digital signal processor reads out the CCD and prepares the images for telemetry to ground. For this mission ion images were acquired 83 times per second.

[11] A number of ground-based instruments were operated in support of the flight; here we summarize only those relevant to this paper. Ionospheric convection maps were obtained at a 2 minute cadence from the CUTLASS SuperDARN radars at Hankasalmi and Þykkvibær running in stereo mode [*Lester et al.*, 2004]. The 42 m EISCAT Svalbard Radar (ESR), located at an altitude-adjusted corrected geomagnetic (AACGM) latitude of 75.1°, observed electron density, electron temperature, ion temperature, and line-of-sight ion bulk flow along the geomagnetic field direction.

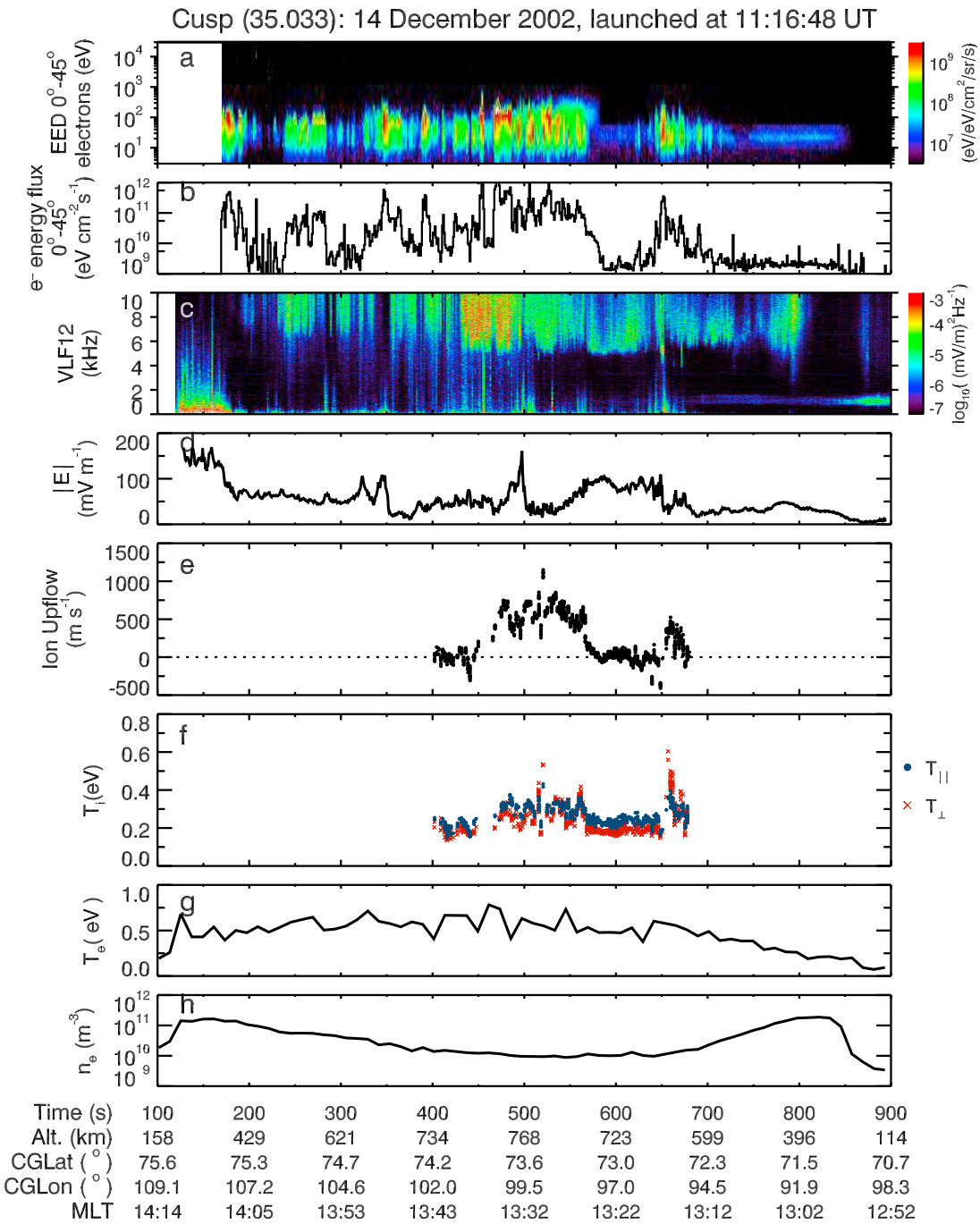

Figure 2. In situ observations from the 35.033 sounding rocket: (a) cusp field-aligned ($\alpha < 45°$) electron energy-time spectrogram, (b) total electron energy flux, (c) AC electric field sonogram, (d) magnitude of DC-coupled electric field, (e) ion upflow (antiparallel to $\vec{B}_0$), (f) ion temperatures parallel and perpendicular to $\vec{B}_0$, (g) electron temperature, and (h) electron density.

2.2. Flight Overview

[12] Figure 2 presents an overview of the rocket observations plotted against time, altitude, corrected geomagnetic latitude and longitude, and magnetic local time. Figure 2a is an energy-time spectrogram of downgoing (pitch angle $\alpha < 45°$) electrons. Patches of enhanced low-energy (~10–200 eV) electron precipitation, characteristic of magnetosheath electrons, are the dominant feature of the precipitation. Figure 2b shows the total electron energy flux; this quantity will be used to examine the relationship between ion upflow and electron precipitation in section 3.

[13] Figure 2c is a frequency-time spectrogram of the AC-coupled electric field signal measured with the spin plane ($\perp\vec{B}_0$) double probe (spheres 1 and 2). The main feature is the VLF hiss emission above 5 kHz. Also evident are BBELF emissions up to a few kHz which shut off

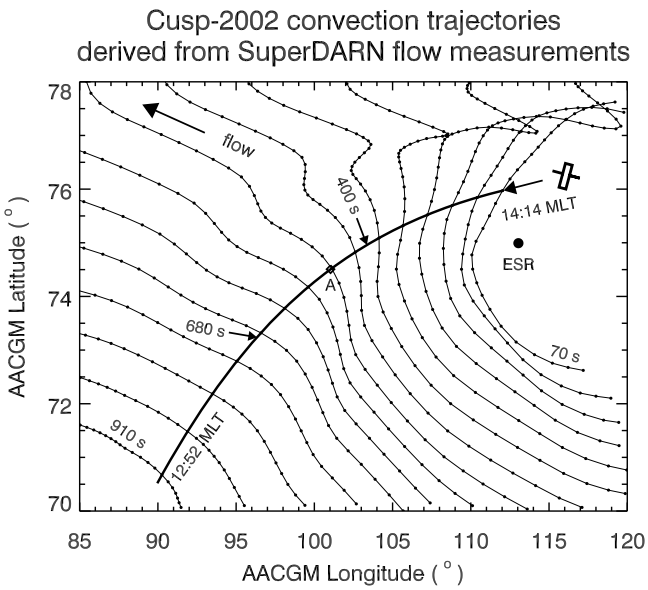

Figure 3. Magnetic footprint of the payload (thick, solid curve) and test particle trajectories (thin, dotted curves derived from SuperDARN CUTLASS radar observations) showing the time evolution of ionospheric convection antisunward from bottom right to top left. "ESR" marks the location of the EISCAT Svalbard Radar. Apogee is marked with the asterisk labeled "A." Labels "910 s" and "70 s" at the far left and right of the plot, respectively, indicate the time in seconds after launch that the corresponding test particle intercepts the payload. Labels "400 s" and "680 s" mark the beginning and end, respectively, of the SII data interval of Figure 2. The magnetic local times of these interceptions are marked "MLT." Dot spacing is 20 s. At its closest point, the rocket came within 1° of latitude and 1.5° of longitude of the ESR.

abruptly at 700 s. The emissions before 200 s are beyond the scope of this paper.

[14] Plotted in Figure 2d is the magnitude of the DC-coupled electric field, $|\vec{E}|$, in the Earth's corotating frame. The convection fields were highly dynamic during the flight: considerable structure is evident in $|\vec{E}|$ during the period 300–700 s after launch.

[15] Figure 2e shows the component of ion velocity in the anti-field-aligned direction (ion upflow) estimated from individual SII energy/angle distributions. For reasons described below, analysis of SII data is limited to the period 400–680 s after launch. Two upflow events are evident: one between 470 and 575 s centered near apogee reaching speeds of 1 km s^{-1}, and a narrower one of less than 500 m s^{-1} between 660 and 680 s at ~670–630 km altitude. Significant downflows are observed before each upflow event. Estimates of mean thermal ion energies (i.e., temperatures) parallel ($T_{i\|}$) and perpendicular ($T_{i\perp}$) to the geomagnetic field are shown in Figure 2f. Isotropic temperatures hovered near 0.2–0.3 eV for most of this event. As will be discussed in section 3, the somewhat anisotropic temperature enhancements within the upflow regions do not correlate with any of the irregularities seen in the AC electric field. Detailed analysis of the ion upflow and temperature are presented in Appendix A.

[16] Electron temperatures obtained from the Langmuir probe are shown in Figure 2g. Compared with typical electron temperatures in the topside polar ionosphere, the electron temperature was elevated and variable throughout most of the flight.

[17] Figure 2h summarizes the electron density measurements estimated from the Langmuir probe. At apogee the density was about 1×10^{10} m^{-3}. The payload crossed the peak of the F region ionosphere at an altitude between 300 and 400 km.

2.3. Supporting Observations

[18] The evolution of the ionospheric convection flows traversed by the payload is presented in Figure 3. Shown are test particle convection trajectories (thin, dotted curves) derived from the SuperDARN CUTLASS radar measurements, along with the footprint of the payload (thick, solid curve), in AACGM coordinates. The flows and the payload track are mapped to a common altitude of 325 km. Apogee is marked with the diamond labeled "A." The test particle trajectories were obtained by interpolating successive 2 minute SuperDARN velocity field maps backward and forward in time at 20 s intervals from points located every 60 s along the rocket trajectory. Labels "910 s" and "70 s" at the far left and right of the plot, respectively, indicate the time in seconds after launch that the corresponding test particle intercepts the payload. For example, the test particle that intercepted the payload at 70 s traversed from 72.6°N × 117.5°E at 1112:58 UT to 77.6°N × 119.3°E at 1122:38 UT, and the test particle that intercepted the payload at 910 s traversed from 70.1°N × 91.5°E at 1129:58 UT to 71.6°N × 85.0°E at 1136:18 UT. For reference the magnetic local times of these two interceptions are indicated by the MLT labels. Labels "400 s" and "680 s" mark the beginning and end, respectively, of the SII data interval of Figure 2. The trajectories represent the average convective motion on time scales of minutes; it is clear from the in situ measurements shown in Figure 2d that the convection electric fields were highly dynamic during the flight. The ionospheric convection pattern showed a number of dynamic features associated with changes in magnetopause reconnection and changes in the IMF, but overall the convection was typical of that in the dayside section of the dusk convection cell of an asymmetric twin cell convection pattern with predominantly antisunward and westward flows, with some eastward flows observed early in the rocket flight in the north east. In crossing from the region of eastward flow to the region of westward flow, the payload made the transition from open field lines characterized by high radar spectral widths, to closed field lines with lower spectral widths.

[19] Altitude-time plots of the ionospheric parameters measured by the ESR are shown in Figure 4. From top to bottom the panels show electron density, electron temperature, ion temperature, and bulk ion flow in the direction of the geomagnetic field. ESR data were averaged in time using a 128 s sliding window. The transient enhancements in electron density and temperature are signatures of electron precipitation, either pulsed in time, or passing through the radar's field of view. The ion temperature occasionally reaches ~0.3 eV, and the bulk ion upflow reaches ~200 m s^{-1}. The enhanced ion temperature and upflow enhancements seen in Figure 4 are qualitatively consistent with the in situ

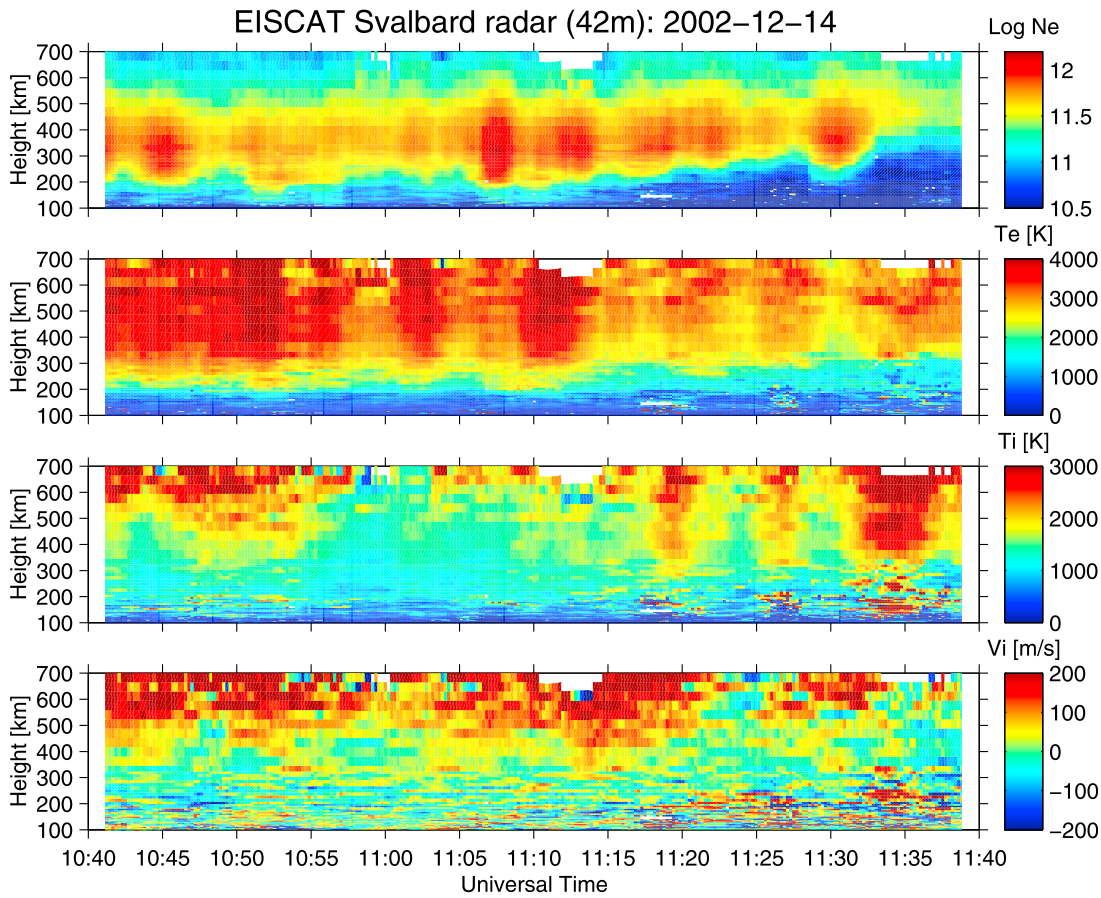

Figure 4. Svalbard Radar observations around the time of the Cusp-2002 rocket flight. From top to bottom: electron density, electron temperature, ion temperature, and ion flow parallel to the geomagnetic field direction. Positive flow values represent bulk ion motion away from the Earth.

observations of Figure 2, even though the payload and ESR measurements were sampled in different volumes.

2.4. Ion Energy/Angle Images

[20] Inspection of the full SII data set has revealed that the highest-quality ion images are obtained when the SII aperture has an unobstructed view of the flowing plasma. Therefore we have selected for analysis rocket spin angles for which the entrance aperture plane is within ±20° (for ion upflow analysis) and ±10° (for ion temperature analysis) of the component of rammed flow (in the payload frame) that is perpendicular to the spin axis. We have excluded images that show evidence of contamination due to detector saturation, and we have used housekeeping monitor data to eliminate images obtained during attitude control system maneuvers and anomalous fluctuations from the high-voltage power supply. Due to an anomaly, sunlight contamination was evident in the SII images; we have corrected this effect by removing a thin-plate spline fit to the smoothly varying contamination, leaving the relatively structured ion signal intact. Thus the ion upflow velocity and temperature measurements presented in this paper are based on cleaned, spin-phase-limited ion images between 400 s and 680 s.

[21] Figure 5 shows the payload altitude versus time along with representative examples of the ion data before (T + 427.137 s) (Figure 5a), within (T + 509.277 s) (Figure 5b), and after (T + 600.627 s) (Figure 5c) the large upflow event near apogee shown in Figure 2d. Assuming the ions are singly ionized, the dashed circular fiducials represent kinetic energies of 2 eV and 10 eV. The projection of the magnetic field in the imaging plane is shown by the arrow labeled "B." The upflow measurements depend on knowledge of the rotation and center of the SII coordinate system, which were calibrated in the lab (from images of N_2^+ ion beams) and again in flight. The intensity scale is linear in pixel count rate, and the white contour levels have equal spacings in count rate. Each image was integrated for approximately 12 ms. The component of the payload motion $v_{r\|}$ antiparallel to $\vec{B}_0$ is shown for each case.

[22] The ion signal in Figure 5a is displaced predominantly laterally along the positive v_x axis, and slightly downward along the negative v_y axis. The lateral displacement results from a combination of the motion of the rocket payload across geomagnetic field lines and an electrical bias of the SII's skin of −2 V with respect to the payload potential Φ_{payload}. The purpose of the skin bias is to ensure that the analyzer acquires ion signal by presenting an attractive potential to the ions, and it results in a minimum kinetic energy per unit charge for the detected ions. The radial and azimuthal spread of the ion signal is a convolution of the thermal width of the ion distribution with focusing and scattering properties of the detector. The difference in

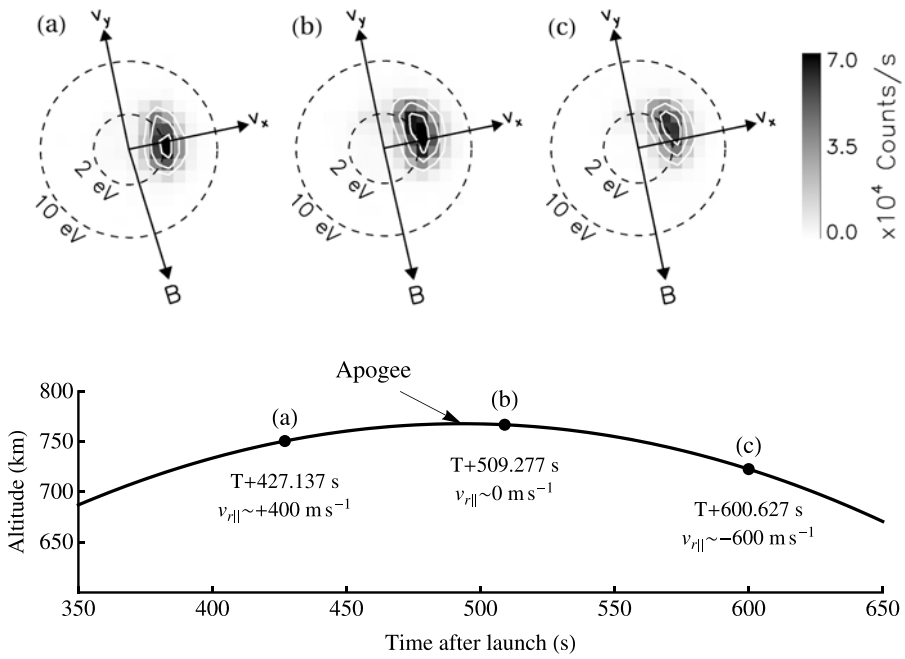

Figure 5. Payload altitude versus time and representative ion images (a) before (T + 427.137 s), (b) within (T + 509.277 s), and (c) after (T + 600.627 s) the large upflow event near the payload apogee. Assuming singly ionized ions, the dashed circular fiducials represent kinetic energies 2 eV and 10 eV. The projection of the magnetic field in the imaging plane is shown by the arrow labeled "B." The intensity scale is linear in pixel count rate, and the white contour levels have equal spacings in count rate. The component of the payload motion $v_{r\|}$ antiparallel to $\vec{B}_0$ is shown for each case.

the x and y widths of the signal is partly an effect of the skin biasing, but we will show later that the ion temperatures perpendicular and parallel to $\vec{B}_0$, respectively, can be derived from these widths; it is these temperatures that are summarized in Figure 2f. The center of the signal is positioned slightly below the v_x axis; since the v_y axis is approximately antiparallel to $\vec{B}_0$, this signal represents an ion distribution that, in the instrument frame of reference, has a downward bulk motion of approximately 400 m s^{-1} in the direction parallel to $\vec{B}_0$. At this time, however, the rocket is moving upward at approximately 400 m s^{-1} antiparallel to $\vec{B}_0$, so there is no bulk flow along $\vec{B}_0$ in the frame corotating with the Earth.

[23] In Figure 5b the ion signal is noticeably displaced upward along the v_y axis, which corresponds to an upflow in the rocket frame. This image was obtained just after apogee where the component of the payload's velocity parallel to $\vec{B}_0$ is negligible, so an upflow in the instrument frame represents a bulk upflow of ions antiparallel to $\vec{B}_0$ in the Earth frame. The image shown in Figure 5b corresponds to the >500 m s^{-1} upflow summarized in Figure 2e. We will refer to this upflow feature as the "main upflow event." A second, narrower, upflow event is evident between 660 s and 680 s after launch.

[24] The ion signal in Figure 5c is also displaced upward along the v_y axis, and in the instrument frame corresponds to bulk motion of ~600 m s^{-1} upward. At this time, however, the payload is falling back to Earth with a speed along $\vec{B}_0$ of approximately 600 m s^{-1}, so in the Earth frame there is no upflow. Examining Figure 2e further, we point out (1) a significant amount of scatter in the upflow measurements, on the order of ±100 m s^{-1} or more, and (2) some narrow "downflow" jets near 440 s and 650 s, reaching several hundreds of meters per second toward the F region.

[25] Figure 6 presents a calibration of the ion flow component parallel to the rocket's spin axis to within a constant offset representing the average upflow velocity over the measurement period. The image first moment $\bar{y}$ (equation (A2)) quantifies the mean location of the ion signal along the

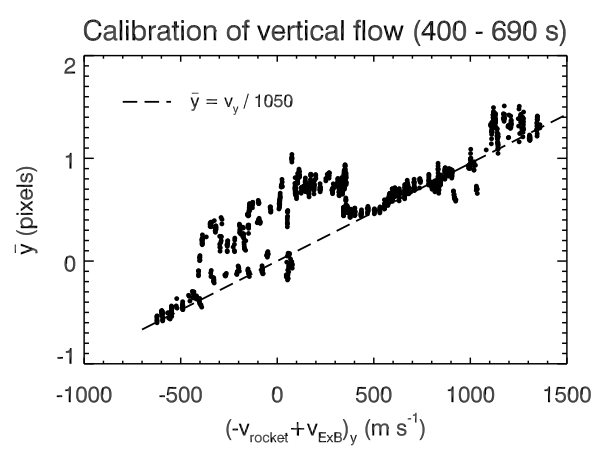

Figure 6. Ion upflow calibration. The dashed line was fit by hand to pass through the (almost) linear parts of the data, namely the intervals from −650 to −400 m s^{-1}, 400 to 1000 m s^{-1}, and 1300 to 1400 m s^{-1}.

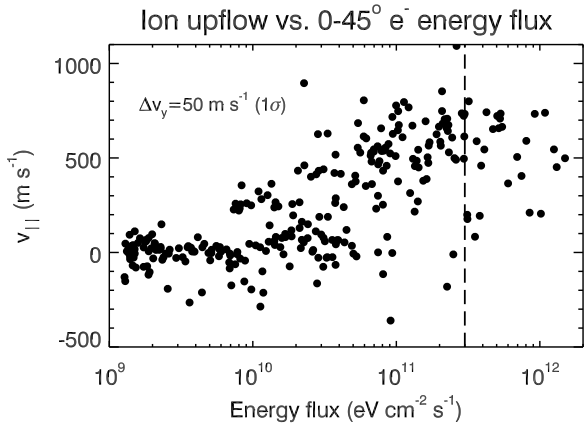

Figure 7. Ion upflow versus 0°–45° electron energy flux. The upflow has been down-sampled to the EED measurement times. The vertical dashed line represents the electron energy flux threshold at which the spacecraft potential begins to significantly affect the upflow measurement. The correlation coefficient for the 162 points corresponding to energy fluxes greater than 1×10^{10} eV cm^{-2} s^{-1} and less than 3×10^{11} eV cm^{-2} s^{-1} is $R = 0.62$.

sensor's v_y axis. As shown in Appendix A, $\bar{y}$ is proportional to the component of bulk ion velocity along the v_y axis in the instrument frame. This bulk ion motion consists mostly of ram flow due to the motion of the rocket through the plasma, and partly of $\vec{E} \times \vec{B}$ drift due to the small (a few degrees) misalignment between the spin axis and the direction of $\vec{B}_0$. Lacking an independent measurement of the ion upflow we assume that the average upflow is zero and fit a straight line by hand to pass through the (almost) linear parts of the data. Details on obtaining ion upflows and temperatures from the ion images, including error analysis, are presented in Appendix A.

3. Results

[26] To investigate the electrodynamics of the ion upflow shown in Figure 2, in this section we examine its relationship to the precipitating electron energy flux, the convection electric field magnitude, the total AC electric field wave power, and the ion temperatures.

[27] The main result of this paper is based on the relationship between ion upflow and energy flux Γ_e of downgoing soft electrons, plotted on a log linear scale in Figure 7. Since the electron energy flux measurements were obtained at a lower cadence than the ion upflow measurements, we have down-sampled the ion data at the EED measurement times. The vertical dashed line is reproduced from Figure A4 and shows the energy flux above which the upflow measurements may be significantly affected by payload potential (see section A3 for an explanation of the effect of payload potential on the ion measurements). Inspection of the plot indicates a clear relation between $v_{\|}$ and $\log_{10}\Gamma_e$. The correlation coefficient (i.e., Pearson R) of the 162 points in the range $1–30 \times 10^{10}$ eV cm^{-2} s^{-1} is $R = 0.62$, which by itself is not conclusive but is consistent with the obvious trend seen in Figure 7. A straight line model least absolute deviation fit of the upflow versus logarithm of the energy flux over the range $1–30 \times 10^{10}$ eV cm^{-2} s^{-1} gives

$$v_{\|}\left(\mathrm{m\,s^{-1}}\right) \sim -4920 + 491 \times \log_{10}\Gamma_e\left(\mathrm{eV\,cm^{-2}\,s^{-1}}\right). \quad (1)$$

For comparison, a linear model between upflow and energy flux gives $v_{\|}$ (m s^{-1}) $= 1.7 \times 10^2 + 2.1 \times 10^{-9}\Gamma_e$ (eV cm^{-2} s^{-1}); the correlation for this model is 10% smaller (R = 0.56). In the analysis that follows we have excluded the small population of data points corresponding to $\Gamma_e \geq 3 \times 10^{11}$ eV cm^{-2} s^{-1} for which payload potential effects may be important.

[28] In Figure 8 we note a tendency for the largest ion upflows to be associated with the smallest DC electric fields. This is opposite to what one would predict if ion upflow were driven by frictional heating from large convection electric fields in the E region ionosphere below the payload.

[29] Next we examine plasma waves as a possible driver of ion upflow. Figure 9 shows that there are small but statistically significant associations between ion upflow and the logarithm of the total wave power (measured from the EFE 1–2 double probe) in each of the following frequency bands: VLF hiss, 5–10 kHz (Figure 9a); broadband ELF (BBELF), 0–1 kHz (Figure 9b); O^+ cyclotron frequencies, 30–50 Hz (Figure 9c); and H^+ cyclotron frequencies, 600–640 Hz (Figure 9d). The correlation is highest for the VLF hiss band (R = 0.33, $5 < f < 10$ kHz), and lowest for the H^+ cyclotron band (R = 0.27, $0 < f < 1$ kHz). The correlations are each based on 67 data points; the smallest (R = 0.27) is significant at the 97% confidence level.

[30] Figure 10a reveals that there is a systematic variation of $T_{i\|}$ with ion upflow (R = 0.81 for 687 points). The same trend is exhibited by $T_{i\perp}$ (Figure 10b, R = 0.70). If indeed it is a real effect, it suggests that there is energy flow from the soft electrons to the ionospheric ions in the form of heat. A possible explanation lies in the plasma waves generated by the electron beam: the larger upflows correspond to ions that may have been accelerating for longer periods, and have therefore had more time to interact with beam-driven plasma waves, resulting in higher temperatures. The apparent lack of a strong correlation between upflow and wave power in

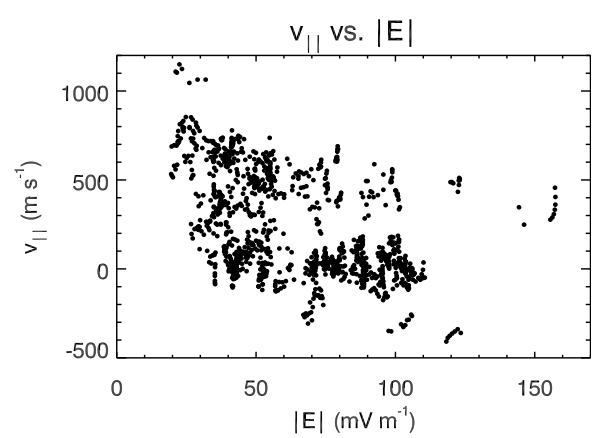

Figure 8. Relationship between ion upflow and $|\vec{E}|$. The correlation coefficient of the 1237 points is −0.48. For the data above 70 mV m^{-1}, R = −0.03; for the data below 70 mV m^{-1}, R = −0.38.

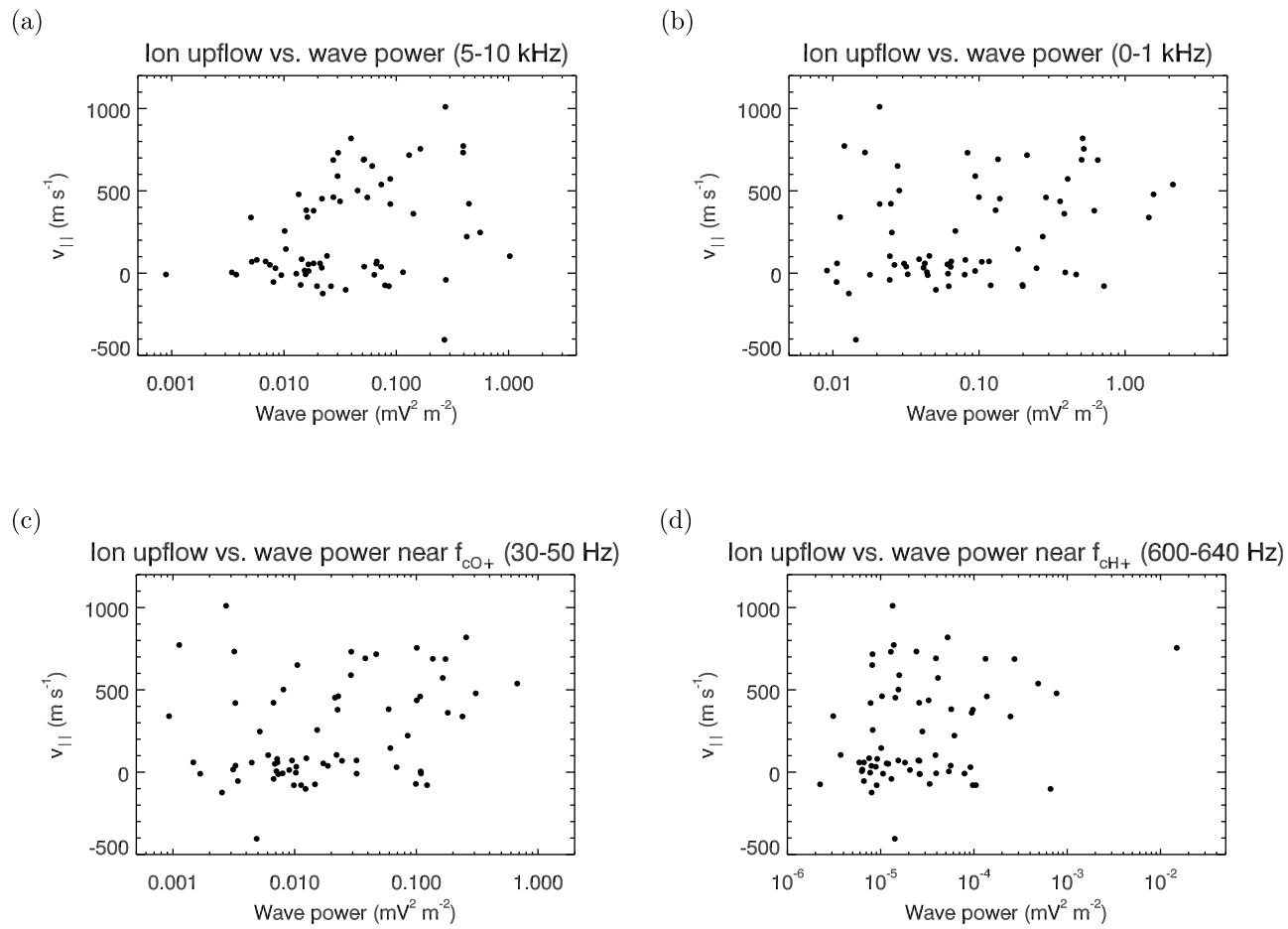

Figure 9. Scatterplots showing ion upflow versus logarithm of total wave power in various bands: (a) VLF hiss, 5–10 kHz (R = 0.33); (b) broadband ELF (BBELF), 0–1 kHz (R = 0.27); (c) O^+ cyclotron frequencies, 30–50 Hz (R = 0.28); and (d) H^+ cyclotron frequencies, 600–640 Hz (R = 0.27).

any of the bands presented above does not preclude this explanation because some of the waves may be of nonlocal origin. Although the underlying trends in Figure 10 are statistically significant, we cannot rule out the possibility that they arise from an uncorrected instrumental effect of unknown origin.

[31] There are clear departures from the trend in Figure 10b, at upflows of 0–500 m s^{-1}. These enhancements are indicative of very weak transverse acceleration of ions.

4. Discussion and Summary

[32] The observations summarized in Figure 2 directly relate the magnitude of ion upflow to the electron energy input into the dayside cusp ionosphere. They are consistent with work by *Wahlund et al.* [1992], *Horwitz and Moore* [1997], *Moen et al.* [2004], and others who have reported a link between electron precipitation and ion upflow in the cusp ionosphere. The absence of significant ion heating and lack of correlation with $|\vec{E}|$ indicates that either the convection electric field does not play a significant role in the upflow for this event, or its influence is buried in the time history of the ionospheric transport. Further study, involving ground-based radar and IMAGE satellite observations, will be needed to determine whether the upflow is caused by enhancements in the ambipolar electric field due to increased ionospheric electron temperature [e.g., *Whitteker*, 1977], by parallel electric fields that arise from plasma instabilities [e.g., *St.-Maurice et al.*, 1996] or conversion of convection electric fields [*Kagan and St.-Maurice*, 2005], or by other physics. Due to overcast sky conditions during the flight, we do not have information to verify the details of the arc geometry and movement that are needed to investigate the details of the upflow mechanism(s). In any case the upflowing ions may possibly reach altitudes above the payload where other energization mechanisms can take hold, leading to escape of ionospheric plasma into the magnetosphere, as suggested by *Bering et al.* [1975], *Shelley et al.* [1982], and others.

[33] *Wilson et al.* [2001] describe the relationship between energetic upward O^+ ion flux and auroral emission in the molecular nitrogen Lyman-Birge-Hopfield long band at 1700 Å in the nightside auroral zone. Based on this association, and the fact that the intensity in the LBH band is proportional to the energy flux of the precipitating electrons, they conclude that "the O^+ escape flux is a function of the precipitating electron energy flux or a closely related quantity." Our Figure 7 illustrates one such functional dependence, albeit our upflows do not represent escape flux.

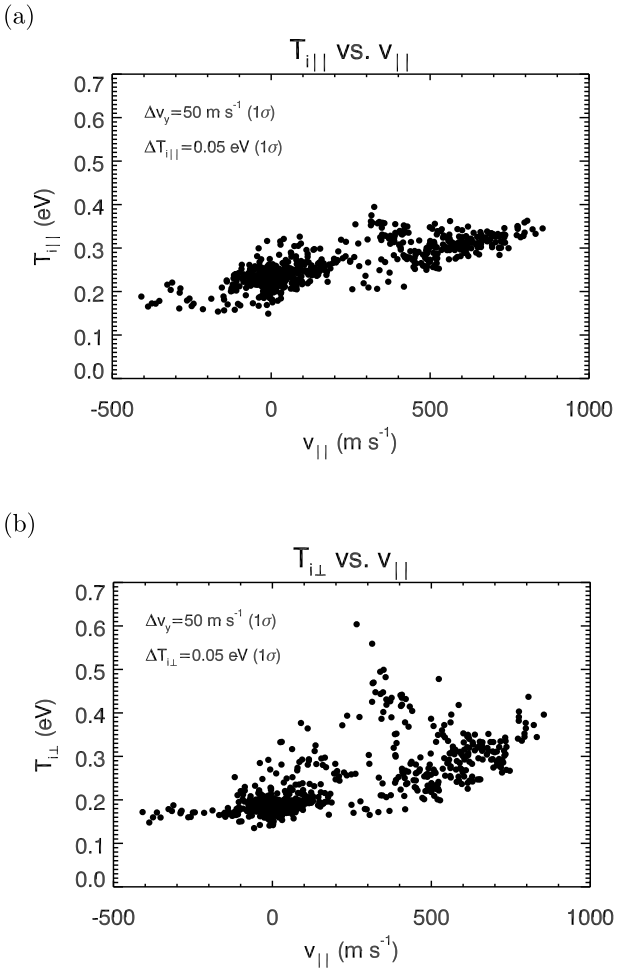

Figure 10. Ion temperature versus upflow. (a) $T_{i\|}$ ($R = 0.81$). (b) $T_{i\perp}$ ($R = 0.70$).

Although their study was in the nightside auroral zone, similar physics may be operating in the dayside cusp.

[34] *Strangeway et al.* [2005] and *Zheng et al.* [2005], using high-altitude satellite observations (4000 km and 6000 km, respectively), found no statistically significant correlation between outflow flux and the energy flux of precipitating electrons. They found instead empirical power law relationships between ion outflow flux and electron density. Scaling our measurements to 4000 km, the correlation for a power law relationship between upflow flux and precipitating electron density [*Strangeway et al.*, 2005, equation (2)] is $R = 0.41$. There are several reasons, however, to expect our results not to be directly comparable with those at high altitude. Our upflow observations do not represent outflow (escape) flux; additional mechanisms, such as acceleration by plasma waves, are needed to explain the high-altitude fluxes. Moreover, as *Strangeway et al.* [2005] and *Zheng et al.* [2005] pointed out, their energy flux measurements included higher-energy electrons which are not as effective at driving upflow as the soft electrons, and this could be expected to diminish the correlations. This point is supported by the Freja satellite observations (at altitudes near 1700 km) of *Knudsen et al.* [1998] (Plate 3, lower left panel) that showed significant correlation between ion energization and precipitating electron number flux only for electron energies less than about 500 eV. The accidentally resonant charge exchange $O^+ + H \rightarrow O + H^+$ [e.g., *Moore*, 1980] also complicates comparisons between low- and high-altitude fluxes. Furthermore, there is the issue of timing, which affects the interpretation of the correlation between ion outflow and electron density summarized in Figure 1 of *Strangeway et al.* [2005]. Soft electrons measured at 4000 km take at most a few seconds to reach the ionosphere, whereas the resulting ion upflows take many tens of minutes to reach altitudes where transverse acceleration of ions by plasma waves dominates the upflow dynamics. Convection of the upflowing ions must, therefore, be a consideration when performing point-by-point correlative studies at high altitudes. Given that Poynting flux, ELF waves, and electron precipitation are all features of the cusp region [e.g., *Strangeway et al.*, 2005], it is possible that some of the high-altitude correlation between ion outflow and electron precipitation is coincidental. Nevertheless, it is clear that soft electrons do influence ion upflow in the cusp topside ionosphere, and the correlations of *Strangeway et al.* [2005], *Zheng et al.* [2005], and *Knudsen et al.* [1998] may be signaling that the ionosphere, as a source of plasma, plays an important role in regulating high-altitude outflow mechanisms.

[35] One explanation for the negative correlation in Figure 8 is that the electric fields are shorted out from enhanced ionospheric conductivity where the electron precipitation is strongest. There is considerable scatter in the data of Figure 8, however, and some of the weaker electric fields may have their origin in other mechanisms.

[36] The correspondence between $v_\|$ and $T_{i\|}$ and $T_{i\perp}$ is qualitatively in agreement with the ground-based radar observations of *Moen et al.* [2004]. Our results are also consistent with *Ogawa et al.* [2000], who found no link between the strength of the convection and ion upflow using ground based radars. The trends in Figure 10 of increasing ion temperatures with upflow velocity are qualitatively similar to Figure 2 (lower panel) of *Seo et al.* [1997], which were obtained using a different measurement technique; this supports the interpretation that these trends are physical and not instrumental in origin.

[37] There is considerable scatter in the upflow measurements. In the case of the SII data, there is inherent noise in the ion upflow and temperature measurements due to photon and MCP pulse height distribution counting statistics [*Knudsen et al.*, 2003]. For the Cusp-2002 SII, counting statistics can account for root-mean-square noise levels in the upflow and ion temperature measurements of 17 m s^{-1} and 0.012 eV, respectively. Variations in spacecraft potential and the analyzer electrode voltages also contribute to the scatter. Moreover, the temporal history and spatial variation of the momentum and energy flows throughout the ionosphere can weaken the correlations between plasma parameters.

[38] The presence of an electron energy flux threshold for the onset of ion upflow may be a clue to the nature of the upflow process. Lower-energy fluxes may drive upflows below the rocket, for example, which do not have enough speed to reach the payload altitude. Further investigation is needed on this aspect of the observations.

[39] It is known that the neutral atmosphere plays a role in ionospheric transport [e.g., *Moore*, 1980; *Lockwood*, 1984],

particularly in view of the CHAMP satellite observations of thermospheric upwelling near the cusp by *Lühr et al.* [2004], and the lower-altitude Streak satellite observations of reduced thermospheric density in the southern cusp by *Clemmons et al.* [2008]. In situ ion upflow and temperature measurements of the kind presented here, coupled with thermospheric measurements, may help in future to elucidate the role of the ionosphere in governing or responding to this redistribution of neutral atmosphere.

[40] This study provides a new perspective on observations of ion upflow in the cusp ionosphere. We summarize the main findings as follows.

[41] 1. There is a positive correlation between the magnitude of the ion upflow and the logarithm of the precipitating magnetosheath electron energy flux (R = 0.62) for fluxes greater than about 10^{10} eV cm^{-2} s^{-1} (Figure 7).

[42] 2. Ion upflow is not observed for electron energy fluxes less than about 10^{10} eV cm^{-2} s^{-1} (Figure 7).

[43] 3. At Cusp-2002 altitudes, the ion upflow does not correlate with convection electric fields greater than 70 mV m^{-1} (R = −0.03). There is a slightly negative correlation (R = −0.38) between ion upflow and $|\vec{E}|$ for field magnitudes less than about 70 mV m^{-1} (Figure 8). One possible explanation for this inverse relationship is that the electron precipitation leads to enhanced ionospheric conductivity and hence weaker electric fields.

[44] 4. Ion upflow correlates weakly with wave power in the VLF (R = 0.33) and BBELF (R = 0.27) bands (Figure 9).

[45] 5. There are positive correlations between ion upflow and the parallel (R = 0.81) and perpendicular (R = 0.70) ion temperatures (Figure 10).

[46] 6. Observations of ion downflows (as large as −400 m s^{-1}) at the downstream edges of the upflow regions are indicative of a return to equilibrium outside the electron precipitation regions (Figure 2).

Appendix A

[47] Here we provide details on the ion image analysis techniques used in this study. For the SII instrument there is not a one-to-one mapping between per pixel count rates and phase space density. This, in combination with instrumental effects such as focusing aberrations, fringing electric fields, and mass ambiguities, makes it impossible to directly invert the ion images into velocity distribution functions. Instead we use a forward modeling technique that simulates ion images by modeling the distribution function and its interaction with the probe. By calculating moments of the simulated images we can characterize the SII's response to a range of ion velocities, temperatures, and floating potentials.

A1. SII Model

[48] We refined the SII model of *Burchill et al.* [2004] by simulating the effect of fringing electric fields within the analyzer on the ion images. Fringing fields arise predominantly near the interface between the entrance window and the gap between the hemispherical electrodes; we calculated the fields by numerically solving (by successive overrelaxation) Laplace's equation for a realistic analyzer geometry and differentiating the potential. We traced particles through the analyzer using an adaptive step-size Runge-Kutta integration scheme. Comparison of model images with flight data showed that the model could be further refined by applying a single radially varying correction for the potential between the analyzing electrodes. At present the physical origin of this correction is not known: it might arise from various effects such as electrode contamination from oxidation, or a small displacement of the inner hemispherical electrode with respect to the outer one, as might happen during the sensor assembly process, for example.

[49] Figure A1a shows a simulation of the SII ion image at 600.627 s (Figure 5c) using a model of the analyzer based on Monte Carlo sampling of a drifting, isotropic Maxwellian O^+ ion velocity distribution function. The Debye sheath around the SII's exterior is modeled using a thin-sheath approximation [*Burchill*, 2003]. Lacking direct measurements of the relative concentrations of various ion species, we assume 100% O^+ for this model; the resulting model images are qualitatively consistent with the flight images (Figure A1a). Due to their larger thermal speeds, the presence of significant amounts of light ions, such as H^+, would cause the ion signal to spread out and cover more of the detector area; we do not observe this effect in any of the flight images. As for other heavy ions, such as N^+, their presence would result in a small correction to the ion velocities and temperatures. As discussed in section 2.4 above, we calibrated the ion upflow measurements, and this calibration will be valid as long as the relative concentrations of various ion species does not vary significantly over the narrow altitude range (~128 km) of the SII measurements throughout the interval of interest.

A2. Ion Image Analysis

[50] Experience has shown that estimates of the ion drift perpendicular to $\vec{B}_0$ are given by x centroids of the image

$$\bar{x} = \frac{1}{S}\sum_{i,j} C_{ij}x_{ij}, \tag{A1}$$

where C_{ij} and x_{ij} are the counts and x position (in pixels), respectively, of the pixel at the intersection of the ith column and jth row, and $S = \Sigma_{i,j} C_{ij}$ is the sum of the image counts. These centroids can be calibrated using the $\vec{E} \times \vec{B}$ drift velocity inferred from measurements of electric and magnetic fields [*Burchill et al.*, 2004; *Sangalli et al.*, 2009]. The Cusp-2002 SII was aligned so that the geomagnetic field lay within a few degrees of the imaging (x, y) plane, which allows us to estimate ion upflows antiparallel to $\vec{B}_0$ from the image first y moments, or y centroids of the image

$$\bar{y} = \frac{1}{S}\sum_{i,j} C_{ij}y_{ij}, \tag{A2}$$

where y_{ij} is the y position of the (i, j)th pixel. Figure A1b illustrates the geometry of the x and y centroids with respect to the SII coordinate system and the ion signal. In the SII coordinate system the direction of the bulk ion drift is represented by the flow angle

$$\phi = \arctan\left(\frac{\bar{y}}{\bar{x}}\right) = \arctan\left(\frac{v_y}{v_x}\right). \tag{A3}$$

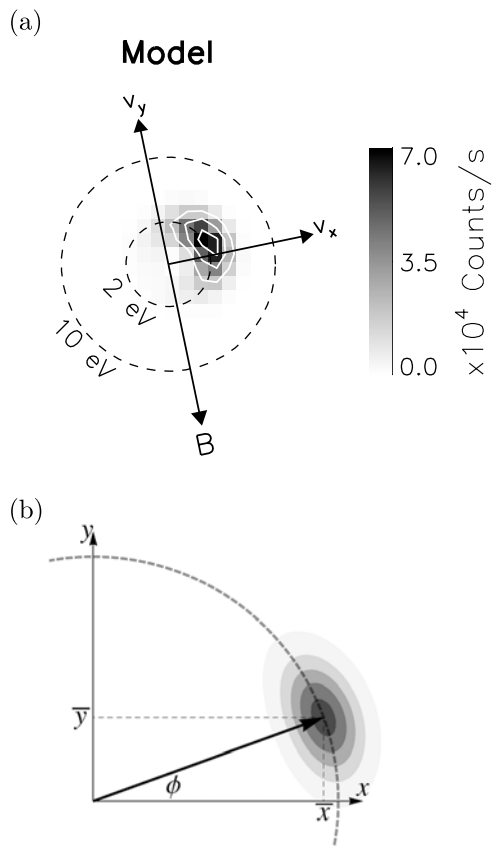

Figure A1. (a) A simulation of the SII ion image at 600.627 s (Figure 5c) using a model of the analyzer based on Monte Carlo sampling of a drifting, isotropic Maxwellian ion velocity distribution function. The simulation parameters are $m_i = 16$ amu, $v_{ix} = 1.60$ km s^{-1}, $v_{iy} = 0.60$ km s^{-1}, $T_{i\perp} = 0.3$ eV, $T_{i\parallel} = 0.3$ eV, and $\Phi_{\text{skin}} = -2.0$ eV. (b) Schematic illustration of ion image first moment geometry.

We will characterize ion temperatures in the directions perpendicular and parallel to the geomagnetic field direction using the second moments of the image

$$x_2 \equiv \overline{(\Delta x)^2} = \frac{1}{S}\sum_{i,j} C_{ij}\left(x_{ij} - \bar{x}\right)^2 \tag{A4}$$

and

$$y_2 \equiv \overline{(\Delta y)^2} = \frac{1}{S}\sum_{i,j} C_{ij}\left(y_{ij} - \bar{y}\right)^2, \tag{A5}$$

where for convenience we name the second x and y moments x_2 and y_2, respectively.

[51] Figure A2 summarizes key dependencies of the first y moment and estimated upflow velocity as determined from simulations. Figure A2a demonstrates that, for constant skin bias voltage, we expect an approximately linear relationship between $\bar{y}$ and $v_\parallel$. The slope of the line depends on the bias voltage and, to a lesser extent, on the ion temperature, but a useful rule of thumb for the Cusp-2002 SII is

$$v_\parallel\left(\text{m s}^{-1}\right) \sim 10^3\bar{y}. \tag{A6}$$

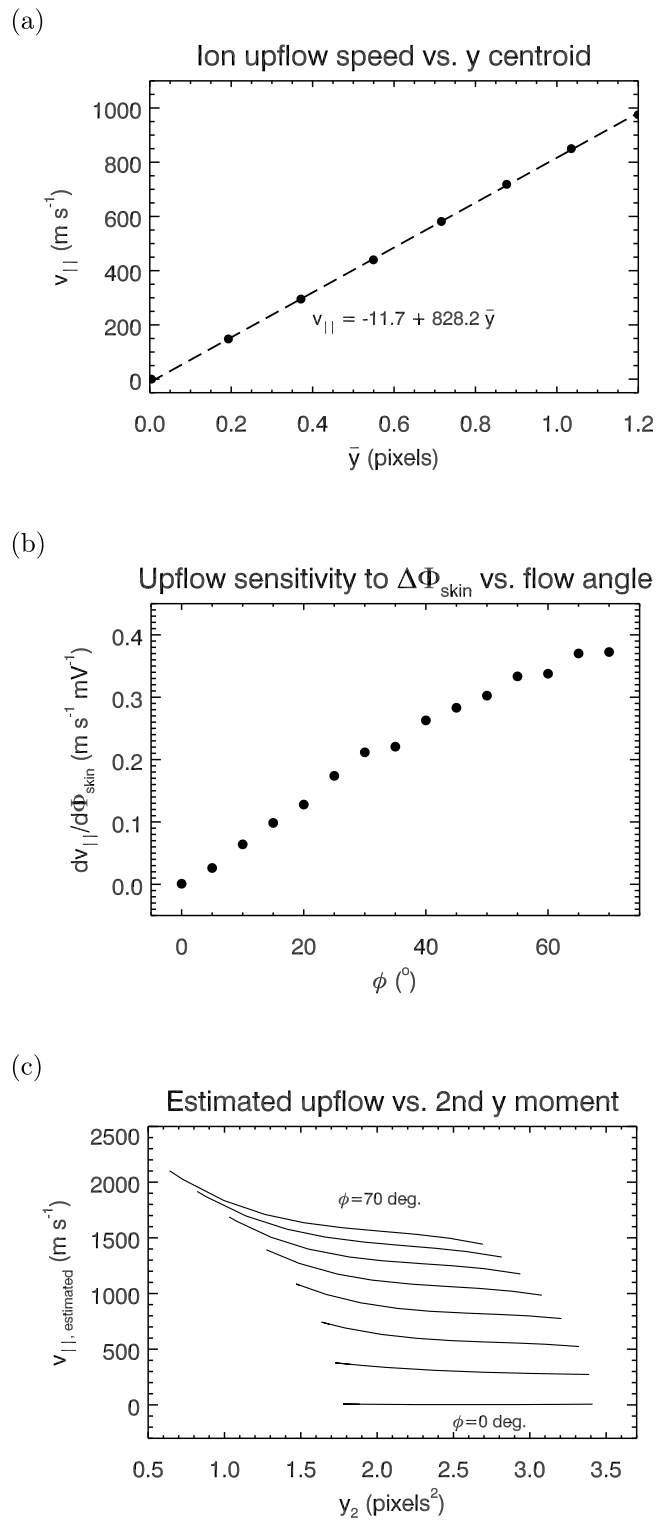

Figure A2. Modeled dependencies of the SII image centroid position $\bar{y}$ and estimated ion upflow $v_\parallel$. (a) Sensitivity of $\bar{y}$ to upflow velocity $v_\parallel$. (b) Rate of change of the estimated upflow with respect to the skin-to-plasma potential Φ_{skin} as a function of flow angle $\phi = \arctan(\bar{y}/\bar{x})$. (c) Dependence of the estimated upflow on the second y moment y_2 for a range of flow angles.

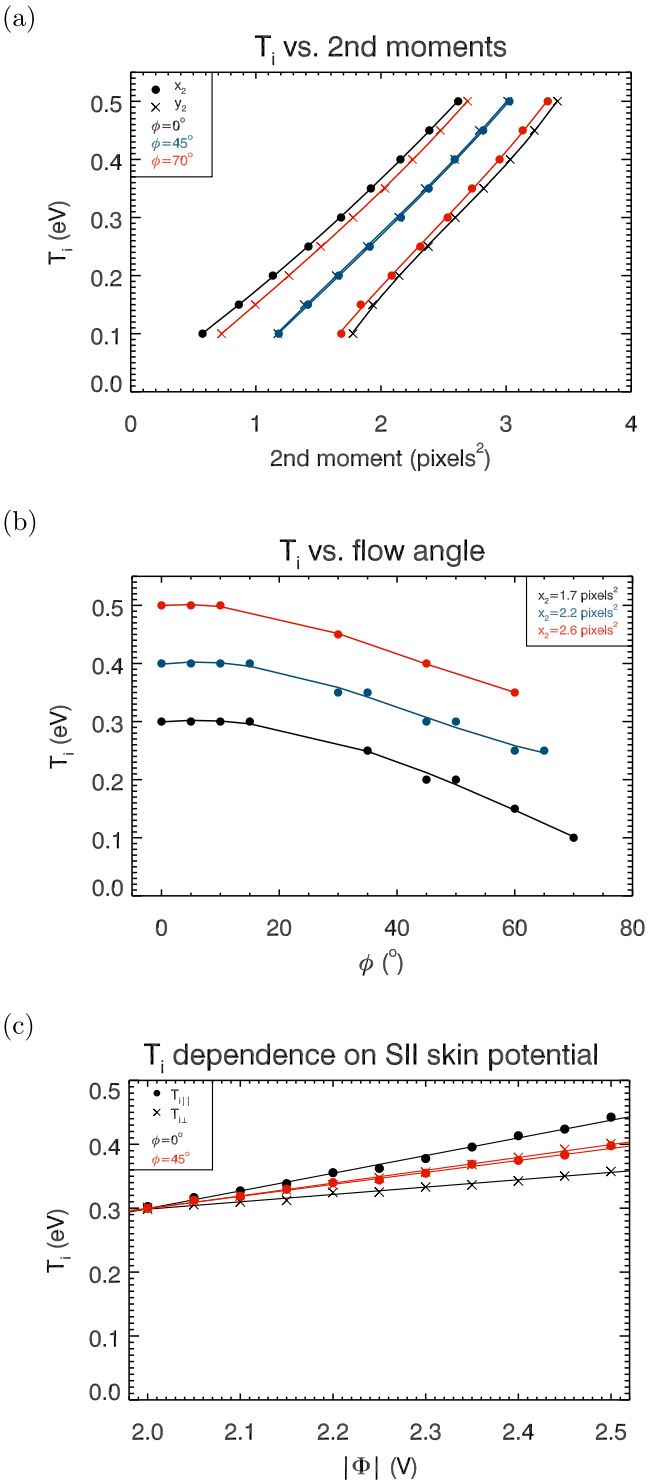

Figure A3. Modeled dependence of ion temperature on (a) image second moments x_2 and y_2 at three different flow angles, (b) flow angle ϕ at three different values of x_2, and (c) the magnitude of the SII skin potential $\Phi_{skin} = \Phi_{payload} - 2.0$ V. The solid curves in Figures A3a and A3b are third-degree polynomial fits to the model values.

Figure A2b shows the modeled sensitivity of the estimated upflow velocity to variations in SII skin-to-plasma potential difference, Φ_{skin}, which is nominally set to $\Phi_{payload} - 2$ V. The response is shown for flow angles ϕ from 0° to 70° in 5° increments. The largest upflows of ~1 km s^{-1} in Figure 2e reach flow angles of 70°, which, according to Figure A2b, can account for a derived velocity error of at most 0.38 m s^{-1} mV^{-1}. Near apogee, where ϕ is typically small, the upflow measurements are practically insensitive to variations in spacecraft potential. There is also a dependence of the estimated upflow on the second y moment, y_2, as shown in Figure A2c. The effect is largest at large flow angles. We corrected the ion upflow estimates for this effect using the measured values for ϕ and y_2.

[52] Figure A3 summarizes the modeled dependence of ion temperature on second moment (Figure A3a), ion flow angle (Figure A3b), and SII skin potential (Figure A3c). In Figure A3a, for a given floating potential and flow angle ϕ there is a well-defined monotonically increasing relationship between T_i and the second x and y moments, which we fit using a polynomial model. The x and y second moments are equal at ϕ = 45°. As shown in Figure A3b, for a given second moment, larger flow angles correspond to smaller ion temperatures. This relationship arises from the non-symmetric shape of the ion signal in the instrument frame, and we can correct for it. As Figure A3c shows, there is a significant dependence of the ion temperature on the payload floating potential. At small flow angles the effect is most pronounced for $T_{i||}$.

A3. Effect of Payload Potential on Upflow Measurement

[53] An important point concerning the interpretation of low-energy ionospheric ion data is that the ions in the plasma frame have kinetic energies per unit charge on the order of, or less than, the electric potential surrounding the payload. It is for this reason that the SII sensor is attached to the payload on a 1 m long boom. Nevertheless, changes in payload potential $\Phi_{payload}$, to which the skin of the SII is electrically biased, affect the ion images. The principal effect of payload potential variations on the ion images is to change the minimum kinetic energy of the detected ions, and this corresponds to variations in mean radial position of the signal $\bar{r} \sim \sqrt{\bar{x}^2 + \bar{y}^2}$. We are assuming that the potential structure around the sensor is cylindrically symmetric about the sensor's z axis. This assumption is justified by the fact that the sensor is mounted on the boom, many tens of Debye lengths away from the payload sheath. It is clear from the ion images in Figure 5 that the flow angles ϕ are typically closer to 0° than 90°, which means that variations in Φ will have a relatively small impact on the parallel flow estimates derived from $\bar{y}$, but will have a much larger impact on perpendicular flows derived from $\bar{x}$. For this reason we have focused on the results derived from the $\bar{y}$, x_2 and y_2 image moments, namely ion upflow and temperatures perpendicular and parallel to $\vec{B}_0$.

[54] Accurate measurements of $\Phi_{payload}$ from the Langmuir probe on 35.033 are not available, and we therefore cannot correct the ion flows for spacecraft potential variations. We can nevertheless quantify the accuracy of our upflow measurements by assessing how much the spacecraft

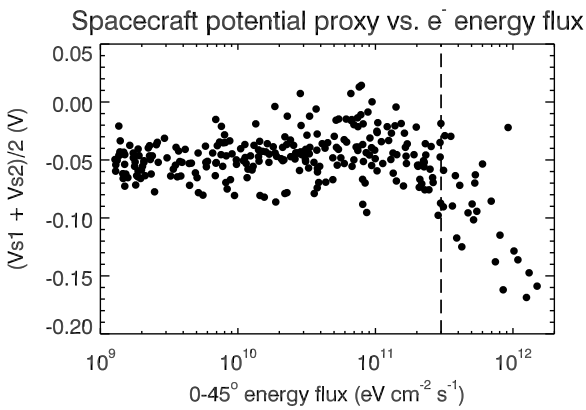

Figure A4. Spacecraft potential proxy versus 0°–45° electron energy flux. The vertical line at 3×10^{11} eV cm^{-2} s^{-1} marks the energy flux above which the spacecraft potential is affected by the precipitation.

potential can vary throughout the ion upflow measurement interval.

[55] Given that (1) the minimum current from ambient electrons with $T_e \sim 0.5$ eV is on the order of $A_T n_e q_e v_{th,e} \sim -0.47 A_T$ mA m^{-2}, where A_T is the total spacecraft area; (2) the electron precipitation has a maximum current on the order of $A_\perp q_e F_{e,\max} \sim -0.016 A_\perp$ mA m^{-2}, where $A_\perp$ is the cross-sectional area of the spacecraft that is seen by the precipitating electrons, and $F_{e,\max} \sim 10^{14}$ m^{-2} s^{-1} is the maximum observed downgoing electron particle flux; and (3) the ratio $A_T/A_\perp$ is certainly greater than 1, it is unlikely that the precipitating electrons can alter the total current to the spacecraft by more than a few percent. From the typical Cusp-2002 Langmuir probe characteristic curve in Figure 3 of *Steigies et al.* [2005], we can relate the changes in total current that are due to the ~10–200 eV precipitating electrons to changes in the floating potential as follows. The probe diameter is 2.5 cm and it has a surface area of about 5 cm^2, which puts the ambient electron current near 0.24 μA. The probe draws approximately this much current when it is at the plasma potential, which on the LP characteristic of *Steigies et al.* [2005] is about 1.4 V with respect to probe ground. Here a change in the current of a few percent corresponds to a change in potential of no more than 200 mV. For the extreme upflows at $\phi = 70°$, and recalling that a change in $\bar{y}$ of 1 pixel corresponds to ~1000 m s^{-1} change in $v_\parallel$, the spacecraft potential variation can account for at most 90 m s^{-1} of the upflow. Given that the preponderance of upflows occur at flow angles of less than 45°, and that most of the precipitating electron flux is less than half its maximum value, we place a conservative $1 - \sigma$ limit of ±50 m s^{-1} on uncertainties in the ion upflow measurements due to variations in precipitating electron flux. The variability in floating potential depends also on the changes in electron density and temperature (we assume that the flux of photoelectrons coming from the payload is relatively constant over the measurement interval), so presumably some of the low-amplitude randomness in the upflow measurements arises from these effects. We assume also that ionospheric photoelectrons do not have enough flux to significantly alter the spacecraft potential.

[56] An estimate for Φ_{payload} can be obtained from the DC-coupled electric field data. V_{S1} (V_{S2}) is the potential difference between the payload and sphere 1 (sphere 2) of the EFE 1–2 antenna (Figure 1). Hence, $V_{S1} + V_{S2}$ is twice the payload potential minus twice the average sphere potentials. Thus, the sum of these potential measurements divided by two may be considered a proxy for the spacecraft potential, provided the sphere potential contribution is relatively small in comparison. Note that for two opposing spheres at equal distances from the spacecraft (such as spheres 1 and 2 in the present study), the potential differences between each sphere and the spacecraft due to the ambient electric field and the $\vec{v} \times \vec{B}$ motional emf are equal and opposite to each other and hence cancel. Figure A4 shows the dependence of this spacecraft potential proxy, $\Phi_{\text{proxy}} = (V_{S1} + V_{S2})/2$, on the precipitating electron energy flux Γ_e. The potential is stable up to an energy flux of ~3×10^{11} eV cm^{-2} s^{-1}, beyond which there is a noticeable drop. Given that the electrons have kinetic energies of approximately 50–100 eV, this suggests that the payload potential is affected by precipitating electrons once the precipitating flux exceeds about 1% of the ambient electron flux, which is on the order of 3.5×10^{11} cm^{-2} s^{-1}. In sections 3 and 4 we have drawn conclusions from ion upflow results for energy fluxes below the threshold where spacecraft potential effects are important.

A4. Ion Temperature

[57] As shown in Figure A3, estimates of ion temperature need to include corrections for the dependence on flow angle and payload potential. We condensed these results into a least squares two-dimensional surface fit of $T_i(x_2, \phi)$ and $T_i(y_2, \phi)$ for $\Phi_{\text{skin}} = -2.0$ V. Because we do not have accurate knowledge of the payload potential, we can only place a limit on the variations in ion temperature presented in Figure 2e using our estimate of the variation in payload potential described above. We assume that the payload potential varies by at most ±100 mV, which corresponds to an uncertainty of ±0.05 eV in the temperature estimates. It is difficult to quantify the uncertainty in the measurement due to the ion distribution being non-Maxwellian. Given that the ESR measurements show ion temperatures near 0.2–0.3 eV (Figure 4), we suggest that the order of magnitude of our ion temperatures is reasonable, but that the smaller-amplitude variations might include some instrumental effects. We note further that outside the upflow regions there is a tendency for $T_{i\parallel}$ to be somewhat larger than $T_{i\perp}$, but since we have no independent in situ measurements it is not possible to determine whether there is a systematic error in one, both, or neither of the ion temperature components.

[58] **Acknowledgments.** This research was supported by the Canadian Space Agency and the Natural Sciences and Engineering Research Council of Canada. The Cusp SII development was supported by a contract from the Canadian Space Agency. The Aerospace Corporation acknowledges NASA support through grant NAG5-5264. The authors acknowledge the contributions and expertise of the SII development team (K. Berg, G. Enno, P. King, C. Marcellus, and I. Wevers) at the Institute for Space Research of the University of Calgary. We would like to thank the PIs of the Northern Hemisphere SuperDARN radars (W. A. Bristow, R. A. Greenwald, T. Kikuchi, M. Lester, M. Pinnock, G. Sofko, and J.-P. Villain) for providing SuperDARN data for this interval. CUSTLASS is a PPARC UK National Facility operated by the University of Leicester. EISCAT is an international scientific association supported by research organizations of China

(CRIRP), Finland (SA), France (CNRS, till the end of 2006), Germany (DFG), Japan (NIPR and STEL), Norway (NFR), Sweden (VR), and the United Kingdom (STFC). J.K.B. appreciates helpful discussions on the ion upflow measurements with W. Peterson, J.-P. St. Maurice, L. Kagan, S. Buchert, B. Jackel, and P. Amerl.

[59] Bob Lysak thanks Eric Lund and another reviewer for their assistance in evaluating this paper.

References

Abe, T., B. A. Whalen, A. W. Yau, R. E. Horita, S. Watanabe, and E. Sagawa (1993), EXOS D (Akebono) suprathermal mass spectrometer observations of the polar wind, *J. Geophys. Res.*, *98*, 11,191–11,203, doi:10.1029/92JA01971.

André, M., P. Norqvist, L. Andersson, L. Eliasson, A. I. Eriksson, L. Blomberg, R. E. Erlandson, and J. Waldemark (1998), Ion energization mechanisms at 1700 km in the auroral region, *J. Geophys. Res.*, *103*, 4199–4222, doi:10.1029/97JA00855.

Banks, P. M., and T. E. Holzer (1969), High-latitude plasma transport: The polar wind, *J. Geophys. Res.*, *74*, 6317–6332, doi:10.1029/JA074i026p06317.

Bering, E. A., M. C. Kelley, and F. S. Mozer (1975), Observations of an intense field-aligned thermal ion flow and associated intense narrow band electric field oscillations, *J. Geophys. Res.*, *80*, 4612–4620, doi:10.1029/JA080i034p04612.

Bouhram, M., et al. (2002), Ion outflow and associated perpendicular heating in the cusp observed by Interball Auroral Probe and Fast Auroral Snapshot, *J. Geophys. Res.*, *107*(A2), 1023, doi:10.1029/2001JA000091.

Burchill, J. K. (2003), High-resolution observations of core and suprathermal ions in the auroral ionosphere: Techniques and results from the GEODESIC sounding rocket, Ph.D. thesis, Univ. of Calgary, Calgary, AB, Canada.

Burchill, J. K., D. J. Knudsen, B. J. J. Bock, R. F. Pfaff Jr., D. D. Wallis, J. H. Clemmons, S. R. Bounds, and H. Stenbaek-Nielsen (2004), Core ion interactions with BB ELF, lower hybrid, and Alfvén waves in the high-latitude topside ionosphere, *J. Geophys. Res.*, *109*, A01219, doi:10.1029/2003JA010073.

Carlson, C. W., D. W. Curtis, G. Paschmann, and W. Michel (1982), An instrument for rapidly measuring plasma distribution functions with high resolution, *Adv. Space Res.*, *2*, 67–70, doi:10.1016/0273-1177(82)90151-X.

Carlson, C. W., et al. (1998), FAST observations in the downward auroral current region: Energetic upgoing electron beams, parallel potential drops, and ion heating, *Geophys. Res. Lett.*, *25*, 2017–2020, doi:10.1029/98GL00851.

Chappell, C. R. (1988), The terrestrial plasma source: A new perspective in solar-terrestrial processes from Dynamics Explorer, *Rev. Geophys.*, *26*, 229–248, doi:10.1029/RG026i002p00229.

Cladis, J. B. (1986), Parallel acceleration and transport of ions from polar ionosphere to plasma sheet, *Geophys. Res. Lett.*, *13*, 893–896, doi:10.1029/GL013i009p00893.

Clemmons, J. H., J. H. Hecht, D. R. Salem, and D. J. Strickland (2008), Thermospheric density in the Earth's magnetic cusp as observed by the Streak mission, *Geophys. Res. Lett.*, *35*, L24103, doi:10.1029/2008GL035972.

Frederick-Frost, K. M., K. A. Lynch, P. M. Kintner Jr., E. Klatt, D. Lorentzen, J. Moen, Y. Ogawa, and M. Widholm (2007), SERSIO: Svalbard EISCAT rocket study of ion outflows, *J. Geophys. Res.*, *112*, A08307, doi:10.1029/2006JA011942.

Ganguli, G., M. J. Keskinen, H. Romero, R. Heelis, T. Moore, and C. Pollock (1994), Coupling of microprocesses and macroprocesses due to velocity shear: An application to the low-altitude ionosphere, *J. Geophys. Res.*, *99*, 8873–8889, doi:10.1029/93JA03181.

Ghielmetti, A. G., R. G. Johnson, R. D. Sharp, and E. G. Shelley (1978), The latitudinal, diurnal, and altitudinal distributions of upward flowing energetic ions of ionospheric origin, *Geophys. Res. Lett.*, *5*, 59–62, doi:10.1029/GL005i001p00059.

Gorney, D. J., A. Clarke, D. Croley, J. Fennell, J. Luhmann, and P. Mizera (1981), The distribution of ion beams and conics below 8000 km, *J. Geophys. Res.*, *86*, 83–89, doi:10.1029/JA086iA01p00083.

Heelis, R. A., and W. B. Hanson (1998), Measurements of thermal ion drift velocity and temperature using planar sensors, in *Measurement Techniques in Space Plasmas: Particles*, *Geophys. Monogr. Ser.*, vol. 102, edited by R. F. Pfaff, J. E. Borovsky, and D. T. Young, pp. 61–71, AGU, Washington, D. C.

Hoffman, J. H., and W. H. Dodson (1980), Light ion concentrations and fluxes in the polar regions during magnetically quiet times, *J. Geophys. Res.*, *85*, 626–632, doi:10.1029/JA085iA02p00626.

Horwitz, J. L. (1982), The ionosphere as a source for magnetospheric ions, *Rev. Geophys.*, *20*, 929–952.

Horwitz, J. L., and T. E. Moore (1997), Four contemporary issues concerning ionospheric plasma flow to the magnetosphere, *Space Sci. Rev.*, *80*, 49–76.

Kagan, L. M., and J.-P. St.-Maurice (2005), Origin of type-2 thermal-ion upflows in the auroral ionosphere, *Ann. Geophys.*, *23*, 13–24.

Knudsen, D. J., J. H. Clemmons, and J.-E. Wahlund (1998), Correlation between core ion energization, suprathermal electron bursts, and broadband ELF plasma waves, *J. Geophys. Res.*, *103*, 4171–4186, doi:10.1029/97JA00696.

Knudsen, D. J., J. K. Burchill, K. Berg, T. Cameron, G. A. Enno, C. G. Marcellus, E. P. King, I. Wevers, and R. A. King (2003), A low-energy charged particle distribution imager with a compact sensor for space applications, *Rev. Sci. Instrum.*, *74*, 202–211, doi:10.1063/1.1525869.

Lester, M., et al. (2004), Stereo CUTLASS: A new capability for the SuperDARN HF radars, *Ann. Geophys.*, *22*, 459–473.

Liu, C., J. L. Horwitz, and P. G. Richards (1995), Effects of frictional ion heating and soft-electron precipitation on high-latitude *F*-region upflows, *Geophys. Res. Lett.*, *22*, 2713–2716, doi:10.1029/95GL02551.

Lockwood, M. (1984), Thermospheric control of the auroral source of O^+ ions for the magnetosphere, *J. Geophys. Res.*, *89*, 301–315, doi:10.1029/JA089iA01p00301.

Lockwood, M., M. Chandler, J. Horwitz, J. Waite Jr., T. Moore, and C. Chappell (1985), The cleft ion fountain, *J. Geophys. Res.*, *90*, 9736–9748, doi:10.1029/JA090iA10p09736.

Loranc, M., and J.-P. St.-Maurice (1994), A time-dependent gyro-kinetic model of thermal ion upflows in the high-latitude *F* region, *J. Geophys. Res.*, *99*, 17,429–17,452, doi:10.1029/93JA01852.

Loranc, M., W. B. Hanson, R. A. Heelis, and J.-P. St.-Maurice (1991), A morphological study of vertical ionospheric flows in the high-latitude *F* region, *J. Geophys. Res.*, *96*, 3627–3646, doi:10.1029/90JA02242.

Lühr, H., M. Rother, W. Köhler, P. Ritter, and L. Grunwaldt (2004), Thermospheric up-welling in the cusp region: Evidence from CHAMP observations, *Geophys. Res. Lett.*, *31*, L06805, doi:10.1029/2003GL019314.

Lynch, K. A., J. L. Semeter, M. Zettergren, P. Kintner, R. Arnoldy, E. Klatt, J. Labelle, R. G. Michell, E. A. MacDonald, and M. Samara (2007), Auroral ion outflow: Low altitude energization, *Ann. Geophys.*, *25*, 1967–1977.

Moen, J., K. Oksavik, and H. C. Carlson (2004), On the relationship between ion upflow events and cusp auroral transients, *Geophys. Res. Lett.*, *31*, L11808, doi:10.1029/2004GL020129.

Moore, T. E. (1980), Modulation of terrestrial ion escape flux composition (by low-altitude acceleration and charge exchange chemistry), *J. Geophys. Res.*, *85*, 2011–2016, doi:10.1029/JA085iA05p02011.

Moore, T. E., R. Lundin, D. Alcayde, M. André, S. B. Ganguli, M. Temerin, and A. Yau (1999), Source processes in the high-latitude ionosphere, *Space Sci. Rev.*, *88*, 7–84, doi:10.1023/A:1005299616446.

Nishida, A. (1966), Formation of plasmapause, or magnetospheric plasma knee, by the combined action of magnetospheric convection and plasma escape from the tail, *J. Geophys. Res.*, *71*, 5669–5679.

Ogawa, Y., R. Fujii, S. C. Buchert, S. Nozawa, S. Watanabe, and A. P. van Eyken (2000), Simultaneous EISCAT Svalbard and VHF radar observations of ion upflows at different aspect angles, *Geophys. Res. Lett.*, *27*, 81–84, doi:10.1029/1999GL010665.

Ogawa, Y., S. C. Buchert, R. Fujii, S. Nozawa, and A. P. van Eyken (2009), Characteristics of ion upflow and downflow observed with the European Incoherent Scatter Svalbard radar, *J. Geophys. Res.*, *114*, A05305, doi:10.1029/2008JA013817.

Pfaff, R., C. Steigies, T. Yeoman, S. Milan, M. Lester, P. E. Sandholt, K. Oksavik, J. Clemmons, D. Knudsen, and J. Burchill (2004), Combined sounding rocket and SuperDARN/EISCAT radar observations of plasma convection, shear, irregularities and other phenomena in the cusp, and boundary layer during IMF Bz negative and By negative conditions, paper presented at 35th COSPAR Scientific Assembly, Paris.

Sangalli, L., D. J. Knudsen, M. F. Larsen, T. Zhan, R. F. Pfaff, and D. Rowland (2009), Rocket-based measurements of ion velocity, neutral wind, and electric field in the collisional transition region of the auroral ionosphere, *J. Geophys. Res.*, *114*, A04306, doi:10.1029/2008JA013757.

Semeter, J., C. J. Heinselman, J. P. Thayer, R. A. Doe, and H. U. Frey (2003), Ion upflow enhanced by drifting *F*-region plasma structure along the nightside polar cap boundary, *Geophys. Res. Lett.*, *30*(22), 2139, doi:10.1029/2003GL017747.

Seo, Y., J. L. Horwitz, and R. Caton (1997), Statistical relationships between high-latitude ionospheric *F* region/topside upflows and their drivers: DE 2 observations, *J. Geophys. Res.*, *102*, 7493–7500, doi:10.1029/97JA00151.

Séran, E., H. U. Frey, M. Fillingim, J.-J. Berthelier, R. Pottelette, and G. Parks (2007), Demeter high resolution observations of the ionospheric thermal plasma response to magnetospheric energy input during the magnetic storm of November 2004, *Ann. Geophys.*, *25*, 2503–2511.

Sharp, R. D., R. G. Johnson, and E. G. Shelley (1977), Observation of an ionospheric acceleration mechanism producing energetic keV ions primarily normal to the geomagnetic field direction, *J. Geophys. Res.*, *82*, 3324–3328, doi:10.1029/JA082i022p03324.

Shelley, E. G., R. G. Johnson, and R. D. Sharp (1972), Satellite observations of energetic heavy ions during a geomagnetic storm, *J. Geophys. Res.*, *77*, 6104–6110, doi:10.1029/JA077i031p06104.

Shelley, E. G., W. K. Peterson, A. G. Ghielmetti, and J. Geiss (1982), The polar ionosphere as a source of energetic magnetospheric plasma, *Geophys. Res. Lett.*, *9*, 941–944, doi:10.1029/GL009i009p00941.

Steigies, C., R. F. Pfaff Jr., and D. E. Rowland (2005), Surface property effects on Langmuir probes launched on sounding rockets, in *17th ESA Symposium on European Rocket and Balloon Programmes and Related Research*, edited by B. Warmbein, *Eur. Space Agency Spec. Publ., ESA SP 590*, 331–336.

St.-Maurice, J.-P., W. Kofman, and D. James (1996), In situ generation of intense parallel electric fields in the lower ionosphere, *J. Geophys. Res.*, *101*, 335–356, doi:10.1029/95JA02586.

Strangeway, R. J., R. E. Ergun, Y.-J. Su, C. W. Carlson, and R. C. Elphic (2005), Factors controlling ionospheric outflows as observed at intermediate altitudes, *J. Geophys. Res.*, *110*, A03221, doi:10.1029/2004JA010829.

Tsunoda, R. T., R. C. Livingston, J. F. Vickrey, R. A. Heelis, W. B. Hanson, F. J. Rich, and P. F. Bythrow (1989), Dayside observations of thermal-ion upwellings at 800-km altitude: An ionospheric signature of the cleft ion fountain, *J. Geophys. Res.*, *94*, 15,277–15,290, doi:10.1029/JA094iA11p15277.

Wahlund, J.-E., and H. J. Opgenoorth (1989), EISCAT observations of strong ion outflows from the *F*-region ionosphere during auroral activity: Preliminary results, *Geophys. Res. Lett.*, *16*, 727–730, doi:10.1029/GL016i007p00727.

Wahlund, J.-E., H. J. Opgenoorth, I. Häggström, K. J. Winser, and G. O. L. Jones (1992), EISCAT observations of topside ionospheric ion outflows during auroral activity: Revisited, *J. Geophys. Res.*, *97*, 3019–3037, doi:10.1029/91JA02438.

Waite, J. H., Jr., T. Nagai, J. F. E. Johnson, C. R. Chappell, J. L. Burch, T. L. Killeen, P. B. Hays, G. R. Carignan, W. K. Peterson, and E. G. Shelley (1985), Escape of suprathermal O^+ ions in the polar cap, *J. Geophys. Res.*, *90*, 1619–1630, doi:10.1029/JA090iA02p01619.

Whitteker, J. H. (1977), The transient response of the topside ionosphere to precipitation, *Planet. Space Sci.*, *25*, 773–786, doi:10.1016/0032-0633(77)90129-5.

Wilson, G. R., D. M. Ober, G. A. Germany, and E. J. Lund (2001), The relationship between suprathermal heavy ion outflow and auroral electron energy deposition: Polar/Ultraviolet Imager and Fast Auroral Snapshot/Time-of-Flight Energy Angle Mass Spectrometer observations, *J. Geophys. Res.*, *106*, 18,981–18,994, doi:10.1029/2000JA000434.

Yau, A. W., and M. Andre (1997), Sources of ion outflow in the high latitude ionosphere, *Space Sci. Rev.*, *80*, 1–25, doi:10.1023/A:1004947203046.

Yau, A. W., T. Abe, and W. K. Peterson (2007), The polar wind: Recent observations, *J. Atmos. Sol. Terr. Phys.*, *69*, 1936–1983, doi:10.1016/j.jastp.2007.08.010.

Yeh, H.-C., and J. C. Foster (1990), Storm time heavy ion outflow at mid-latitude, *J. Geophys. Res.*, *95*, 7881–7891, doi:10.1029/JA095iA06p07881.

Zheng, Y., T. E. Moore, F. S. Mozer, C. T. Russell, and R. J. Strangeway (2005), Polar study of ionospheric ion outflow versus energy input, *J. Geophys. Res.*, *110*, A07210, doi:10.1029/2004JA010995.

J. K. Burchill, D. J. Knudsen, and A. W. Yau, Department of Physics and Astronomy, University of Calgary, 2500 University Dr., NW, Calgary, AB T2N 1N4, Canada. (burchill@phys.ucalgary.ca)

J. H. Clemmons, Space Science Applications Laboratory, Aerospace Corporation, 2310 El Segundo Blvd., El Segundo, CA 90245-4691, USA.

K. Oksavik, Department of Arctic Geophysics, University Centre in Svalbard, PB 156, N-9171 Longyearbyen, Norway.

R. F. Pfaff, Space Weather Laboratory, NASA Goddard Space Flight Center, Greenbelt, MD 20771, USA.

C. T. Steigies, Institut für Experimentelle und Angewandte Physik, Christian-Albrechts-Universität zu Kiel, Olshausenstraße 40, D-24098 Kiel, Germany.

T. K. Yeoman, Department of Physics and Astronomy, University of Leicester, Leicester, LE1 7RH, UK.